Magnetite Nanostructured Porous Hollow Helical Microswimmers for Targeted Delivery

*Xiaohui Yan, Qi Zhou, Jiangfan Yu, Tiantian Xu, Yan Deng, Tao Tang, Qian Feng, Liming Bian, Yan Zhang, Antoine Ferreira, and Li Zhang**

Bacteria-inspired magnetic helical micro-/nanoswimmers can be actuated and steered in a fuel-free manner using a low-strength rotating magnetic field, generating remotely controlled 3D locomotion with high precision in a variety of biofluidic environments. They are therefore envisioned for biomedical applications related to targeted diagnosis and therapy. In this article, a porous hollow microswimmer possessing an outer shell aggregated by mesoporous spindle-like magnetite nanoparticles (NPs) and a helical-shaped inner cavity is proposed. The fabrication is straightforward via a cost-effective mass-production process of biotemplated synthesis using helical microorganisms. Here, *Spirulina*-based fabrication is demonstrated as an example. The fabricated microswimmers are superparamagnetic and exhibit low cytotoxicity. They are also capable of performing structural disassembly to form individual NPs using ultrasound when needed. For the first time in the literature of helical microswimmers, a porous hollow architecture is successfully constructed, achieving an ultrahigh specific surface area for surface functionalization and enabling diffusion-based cargo loading/release. Furthermore, experimental and analytical results indicate better swimming performance of the microswimmers than the existing non-hollow helical micromachines of comparable sizes and dimensions. These characteristics of the as-proposed microswimmers suggest a novel microrobotic tool with high loading capacity for targeted delivery of therapeutic/imaging agents in vitro and in vivo.

1. Introduction

Targeted delivery is envisioned as a promising means for diverse biomedical applications such as imaging/diagnostics, gene/cancer therapy, minimally invasive surgery, and so on.[1–5] It aims to maximize the diagnosis/therapy efficacy and minimize undesirable side effects. To this end, a variety of micro-/nanoscale machines and motors, either fuel-driven or fuel-free, have been developed.[3,5–10] Among them, magnetically actuated micro-/nanomotors gain particular interest because of their capability of performing complex maneuvers required by on-demand tasks in an fuel-free and wireless manner using non-invasive magnetic fields.[11,12] Compared with fuel-driven motors, they obviate the requirement of either onboard power systems or detrimental chemical conditions, thus enabling propulsion that causes negligible interference to the physiological environments they navigate. And because their locomotion merely relies on the transmitted power from the input magnetic field, their response to human control can be more robust and precise than magnetically controlled magnetotactic bacteria for cargo loading and transport tasks.

Micro-/nanomotors typically move at low Reynolds number on account of their small dimensions, where inertia is negligible and viscosity dominates.[13] In this regime, effective actuation and steering of the micro-/nanomotors become challenging since regular strokes at the macroscale may fail to generate effective propulsion. Inspired by the flagellar propulsion of *Escherichia coli*,[14] magnetic micro-/nanoswimmers

X. Yan, Q. Zhou, J. Yu, Dr. T. Xu, Q. Feng, Prof. L. Bian, Prof. L. Zhang
Department of Mechanical and Automation Engineering
The Chinese University of Hong Kong
Shatin, N.T., Hong Kong, China
E-mail: lizhang@mae.cuhk.edu.hk
Dr. Y. Deng, Prof. T. Tang
Department of Obstetrics and Gynaecology
The Chinese University of Hong Kong
Shatin, N.T., Hong Kong, China
Q. Feng, Prof. L. Bian, Prof. L. Zhang
Division of Biomedical Engineering
The Chinese University of Hong Kong
Shatin, N.T., Hong Kong, China
Prof. L. Bian, Prof. L. Zhang
Chow Yuk Ho Technology Centre for Innovative Medicine
The Chinese University of Hong Kong
Shatin, N.T., Hong Kong, China
Dr. Y. Zhang
College of Resources and Environment
Qingdao Agricultural University
Qingdao 266109, China
Prof. A. Ferreira
INSA Centre Val de Loire
Laboratoire PRISME
Campus Bourges
88 Boulevard Lahitolle, 18000 Bourges, France

DOI: 10.1002/adfm.201502248

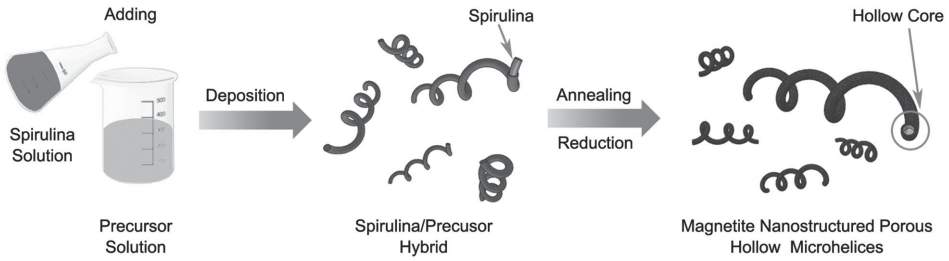

Figure 1. Schematic of the biotemplating process of magnetite nanostructured porous hollow microhelices.

propelled by rotating helical tails have been developed. Methods of fabrication reported in the literature include self-scrolling technique,[7] glancing angle deposition (GLAD),[15] electrochemical processing,[16] 3D lithography[17] and biotemplated synthesis.[18] Using a low-strength rotating magnetic field, the as-fabricated swimmers can be actuated and steered in a controllable fashion and perform precise 3D locomotion in a variety of fluids such as water,[7,15–18] blood,[19] serum[17–19] and biological gel.[20–22] Furthermore, by using biocompatible materials, they can be noncytotoxic.[17,19] To date, significant progress has been achieved by utilizing such swimmers to implement targeted cargo delivery in vitro or in vivo via direct pushing/pulling,[7,15] microfluidic flows/microvortices,[23,24] mechanical confinement,[17] and surface functionalization.[15,25–27]

In this report, we propose a porous hollow helical microswimmer consisting of mesoporous spindle-like magnetite nanoparticles (NPs) toward active targeted delivery of therapeutic/imaging agents in vivo. The fabrication will be demonstrated by the synthesis process of *Spirulina*-templated microswimmers. Likewise, scaled-up or scaled-down microswimmers can be obtained using helical templates of aimed scales. The as-fabricated microswimmers are characterized with optical/fluorescence/ field-emission scanning electron microscopy (FESEM)/transmission electron microscopy (TEM) imaging, energy-dispersive X-ray spectrometer (EDX)/X-ray diffraction (XRD)/thermogravimetric (TG) analysis, vibrating sample magnetometer (VSM) measurement, 3-(4,5-dimethylthiazol-2-yl)-2,5-diphenyltetra-zolium bromide (MTT) assay, N_2 adsorption–desorption test, magnetic actuation, Au-nanorod loading, Rhodamine B (RhB) molecule releasing, and ultrasound treatment. Results reveal that our proposed microswimmer is both superparamagnetic and cytocompatible with excellent steerability. Furthermore, it is featured with three primary advantages for targeted cargo delivery. First, an ultrahigh specific surface area (SSA) is achieved for surface functionalization. Second, a new mechanism of cargo loading/release is enabled based on the porous hollow architecture. Third, the capability of multilevel structural disassembly is acquired with the aid of ultrasound instruments. These desirable properties are intrinsically attributed to the unique micro-/nanostructures of our proposed helical swimmers.

2. Fabrication Process

Of various manufacturing techniques, the method of biotemplated synthesis based on spiral water-conducting vessels of vascular plants has been recently reported as a simple and cost-effective means for mass-production of magnetic helical microswimmers.[18] Besides plants, other organisms have also evolved diverse, sophisticated functional spiral structures of various sizes to adapt to their surrounding environments, thus providing abundant biotemplate options for the synthesis of helical microswimmers.[14,28–31] The cyanobacterium *Spirulina,* a microorganism widely distributed in nature and already commercialized as nutritional supplements or food materials, has drawn considerable attention because of its therapeutic effects for some critical diseases.[32] To our interest, they are naturally of intact helical microstructures featured with a range of parameters needing no post-processing (e.g., the delicate process of extracting spiral vessels from vascular plants in ref.[18]).[33–36] Moreover, their helical features such as helicity and helix diameter are sensitive to their living environments, which can be easily adjusted in cultivation conditions.[33,35,36] This advantage renders it as an ideal candidate for biotemplating process. In our report, the *S. platensis*, one subspecies of the cyanobacterium *Spirulina*, is chosen as a representative to demonstrate the biotemplating synthesis via three steps: precursor deposition, annealing treatment, and reduction processing (**Figure 1**). The fabrication strategy is applicable to other species of cyanobacterium *Spirulina* as well as other biologically helical organisms. For more details of the *S. platensis*, refer to Figure S1 (Supporting Information).

2.1. Deposition of Magnetite Precursor

The first step of *Spirulina*-templated synthesis is deposition of magnetite precursors on the surface of the *S. platensis*, followed by annealing treatment and reduction processing to eventually obtain nanostructured porous hollow magnetic microhelices. In the literature, magnetization of the *S. platensis* has been reported by synthesis using sol–gel method or thermal decomposition.[37,38] The main concern of these methods is the usage of high-risk chemical reagents such as sodium hydroxide, glutaraldehyde, and iron pentacarbonyl. Also, the thickness of the deposited matter on the surface of *S. platensis* could hardly be controlled, which hinders the construction of an advanced architecture possessing hollow-core or porous-shell features. To resolve these issues, we explored substitutes for materials used in the aforementioned methods to conduct the synthesis. $FeCl_2$, $FeCl_3$ solutions, and their mixture, all of which are safe media that have been applied to prepare various magnetite precursors, were chosen as ideal substitutes.[39] Through parametric

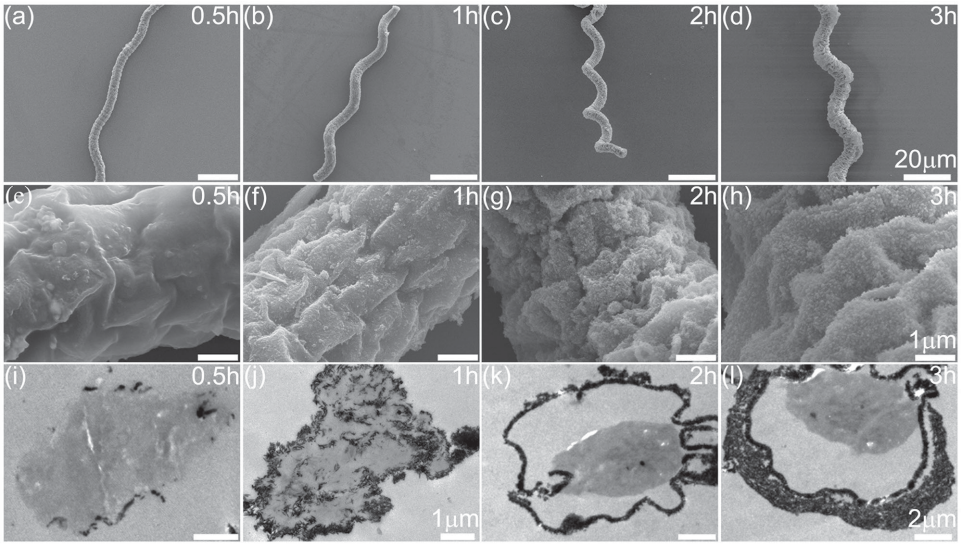

Figure 2. Characterization of the *S. platensis* after precursor deposition in the mixed solution of $FeCl_2$ and $FeCl_3$ (molar ratio, 2:1) for 0.5 h (TS0.5), 1 h (TS1), 2 h (TS2), and 3 h (TS3). a–d) FESEM images of TS0.5, TS1, TS2, and TS3, respectively. e–h) Enlarged views of the samples in a–d). i–l) Cross-sectional bright-field TEM images of the samples, where the high-contrast peripheral areas (in black) are the deposited nanoparticles, and low-contrast central areas (in gray) are the dehydrated *S. platensis*. The scale bars in (a–d) are 20 μm. The scale bars in (e–j) are 1 μm. The scale bars in (k–l) are 2 μm.

experiments (Figure S2, Supporting Information), we were able to identify the optimum conditions for the biotemplated synthesis: in a mixture of $FeCl_2$–$FeCl_3$ (ratio of molar concentration, 2:1) at 65 °C with the protection of ultrahigh-purity N_2; no addictive is needed.

FESEM images of the *S. platensis* treated with the mixed solution as mentioned above for 0.5, 1, 2, and 3 h (referred to as TS0.5, TS1, TS2, and TS3 hereafter) are shown in **Figure 2**a–h, respectively, in which Figure 2a–d indicate that morphological collapse occurred to TS0.5 after dehydration just as what happened to the untreated *S. platensis*, while the helical morphology was basically preserved for TS1 and well preserved for TS2 and TS3. FESEM images of the enlarged areas selected from Figure 2a–d are presented in Figure 2e–h to examine the surface features of TS0.5, TS1, TS2, and TS3, respectively. The quantity of nanoparticles (NPs) deposited on the surface is increased as the dipping time increases. For TS0.5 in Figure 2e, only a small quantity is sparsely deposited. By prolonging the dipping time to 1 h, the deposited NPs become much denser, as illustrated by TS1 in Figure 2f. Eventually, for a dipping time of 2–3 h, a robust and pseudo-homogeneous shell with a large quantity of NPs is formed for TS2 and TS3 as shown in Figure 2g,h. The evolution of the surface feature as described is in good agreement with the biology-induced extracellular mineralization process describing the occurrence of biological deposition on organism surfaces due to metabolism or local environmental changes (e.g., introduction of reactive ligands).[40–43] To determine the chemical composition of the compounds deposited on the surface, we first used EDX, in which Fe element was detected (Figure S3a, Supporting Information). The following XRD test confirmed that the nanomaterial was iron oxide hydrate ($Fe_2O_3 \cdot H_2O$).

Cross-sectional TEM images of TS0.5, TS1, TS2, and TS3, indicating the thickness of the deposited nanomaterial and the core size of the shrunk *S. platensis*, are presented in Figure 2i–l. High-contrast peripheral areas (in black) stand for the deposited matter, and low-contrast central areas (in gray) for the dehydrated *S. platensis*. The size of the core (i.e., the shrunk *S. platensis*) is almost the same and featured as 4–5 μm for all TEM samples, while the thickness of the shell (i.e., the deposited material) grows as the dipping time increases. In other words, the thickness of the deposition can be adjusted in a one-step manner by controlling the processing time. The core–shell architecture can be firmly built within a short period of synthesis time. As shown in Figure 2k,l, for deposition of 2 h and 3 h, the thickness of the shell can reach 250–350 nm and 1–1.5 μm, respectively. The diameter of the shell is estimated to be 9–10 μm, which changes little compared to that of the untreated *S. platensis* (Figure S1a, Supporting Information). It is presumable that the shrinking of the *S. platensis* due to the dehydration contributes to rapid consolidation of the deposited shell, leading to detachment of the shell from the core with little contraction of the cross-section area.[44] Microstructural details of the deposited shell is gained through a high-magnification TEM image, where spindle-shaped mesoporous NPs with 20–70 nm in width and 100–300 nm in length are presented (Figure S3b, Supporting Information).

2.2. Annealing and Reduction

The deposition process was followed by annealing treatment, aimed at fabricating a hollow architecture by removing the *S. platensis* core (Figure S4, Supporting Information). The annealed product (referred to as TS-A hereafter) is in

red-brown powder form (Figure S5c, Supporting Information) with weak magnetization (Figure S5g, Supporting Information), which was determined to be hematite (α-Fe_2O_3) through the XRD test (Figure S5d, Supporting Information). Subsequently, the annealed product was reduced using a hydrogen/argon (volume ratio 1:9) flow so as to obtain magnetite (Fe_3O_4). Attempts under different processing conditions were made, and the optimum condition was 1 h heating at 550 °C. The reduced product (referred to as TS-A-R1 hereafter) was magnetite confirmed by the XRD spectrum (Figure S5f, Supporting Information). Following VSM characterization revealed the Fe_3O_4 shell to be superparamagnetic with a saturation magnetization M_s of 63.48 emu g^{-1} (Figure S6, Supporting Information). This magnetic property suggests that TS-A-R1 is agglomeration-free and will not cause hazardous embolization in human vessels if applied for targeted delivery in vivo.[14,45]

Previously after the first step of deposition, TS1, TS2, and TS3 were able to preserve the helical morphology of the *S. platensis*. However, morphological collapse happened to TS1-A-R1 after annealing and reduction (Figure S7, Supporting Information), while TS2-A-R1 (**Figure 3**) and TS3-A-R1 (Figure S8, Supporting Information) still preserved the morphology well. On the winkled surface of the helices, dense aggregates of spindle-like NPs were observed (Figure 3b and Figure S8b, Supporting Information). The successful construction of a hollow-core architecture for TS2-A-R1 was identified by FESEM imaging of the cross-section (Figure 3c) combined with EDX analysis (Figure S9a, Supporting Information). It is also delineated through comparison between TEM images of TS2-A-R1 and TS2 (Figure 3d and Figure S9b, Supporting Information). The characteristic diameter of the hollow core and thickness of the shell are 8–9 μm and 200–250 nm, respectively. Subsequently, TEM image of the enlarged rectangular area and circular area marked in Figure 3d revealed the existence of large quantities of mesopores (i.e., pores in the range of 2–50 nm) between or on the magnetite NPs aggregated on the shell (Figure 3e,f). The porous hierarchy was analyzed by N_2 adsorption–desorption technique, whose results can yield the SSA and the distribution of pore size through further calculation (Figure S9c,d, Supporting Information). It was found that the density and size of the pores were subject to the annealing treatment, and can be largely affected by the temperature setting and processing time (Figure S10, Supporting Information). Similar structural features as described above for TS2-A-R1 were also found for TS3-A-R1. Conclusively, we have successfully fabricated magnetite helices with porous hollow architecture. And the fabrication process can be easily scaled-up for mass-production of such agents in accord with the procedure provided in the experimental section.

3. Characteristic Properties

3.1. Swimming Performance

Swimming properties of the as-obtained microswimmers were tested using a tri-axial Helmholtz coil system. To be specific, the microswimmers were magnetically actuated and steered by a low-strength rotating magnetic field. Excellent capability of controlled locomotion was observed. As an example, in **Figure 4**, a time-lapse sequence of microscopic images is demonstrated for both the steering and propulsion of TS2-A-R1 (see Figure S11, Supporting Information for the swimmers' geometric parameters). The microswimmer is able to perform wobble-free propulsion and achieve a forward velocity of 64.75 μm s^{-1} with a

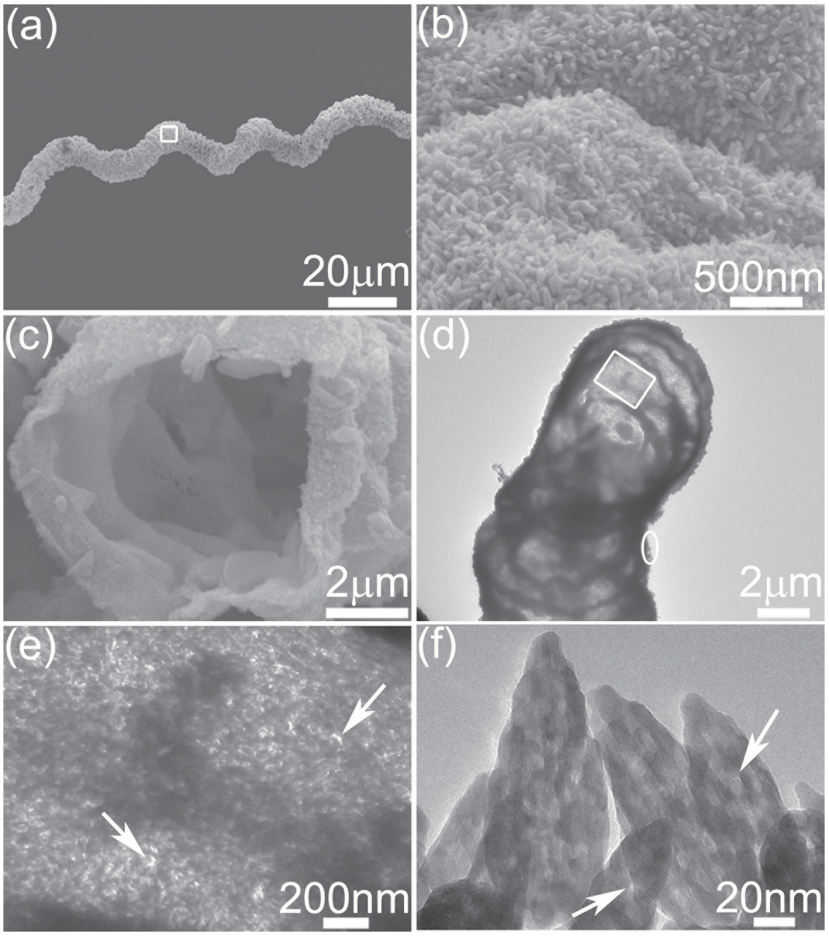

Figure 3. Structural characterization of TS2-A-R1. a) FESEM image of TS2-A-R1. b) Enlarged view of the white rectangle area in (a), showing aggregates of spindle-like nanoparticles. c) Enlarged view of a cross-sectional fracture of TS2-A-R1 after sonication (20 kHz, 0.7 w cm^{-2}) for 1 min in absolute ethanol. d) Bright-field TEM image of TS2-A-R1. e) Enlarged view of the white rectangular area marked in (d), where large mesopores between the nanoparticles are marked with white arrows. f) Enlarged view of the white circular area marked in (d), where small mesopores on individual spindle-shaped nanoparticles are marked with white arrows.

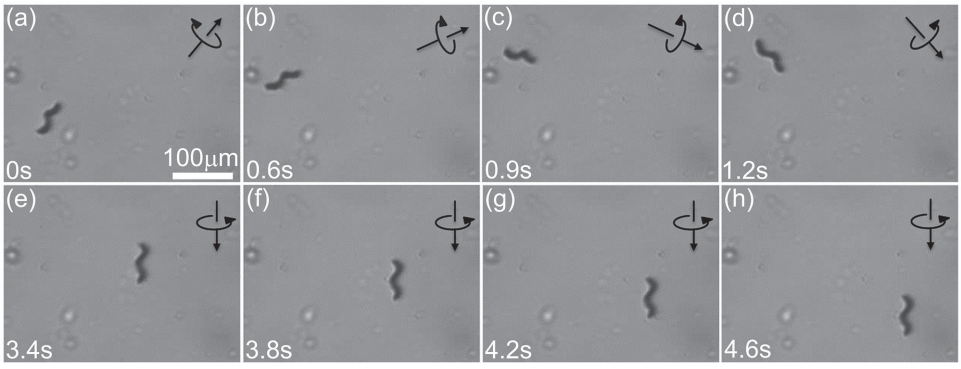

Figure 4. Swimming test of TS2-A-R1 using a low-strength rotating magnetic field. The input strength and rotating frequency are 7 mT and 10 Hz, respectively. a–d) Time-lapse image sequence of the steering with intervals of 0.3–0.6 s. e–h) Time-lapse image sequence of the propulsion with an interval of 0.4 s, where a translation velocity of 64.75 μm s^{-1} can be calculated accordingly. The circular and straight black arrows indicate the rotational and translational directions, respectively. (a–h) share the same scale bar as in (a), which is 100 μm.

moderate rotating frequency of 10 Hz. For more details, the swimming performance is characterized with frequency–velocity relationship in Figure S12 (Supporting Information).

We briefly analyze TS2-A-R1's swimming performance. As mentioned before, TS2-A-R1 was determined to be superparamagnetic. A fundamental difference for the actuation of superparamagnetic microswimmers from that of ferromagnetic ones lies in the fact there is no remanent magnetization for the former. Specifically for helical superparamagnetic swimmers, the propulsive capability was recently revealed to be dominated by two factors: the actuator's effective magnetic susceptibility depending on material category, and its "steerability" controlled by both helix geometry and magnetic property:[46]

$$\mathbf{L}_m = \mathbf{M} \times \mathbf{H} \tag{1}$$

$$\mathbf{M} = \chi \cdot \mathbf{H} V \tag{2}$$

$$\chi_{ik} = \chi_0 \delta_{ik} + \Delta\chi \left(n_i n_k - \frac{1}{3}\delta_{ik} \right) \tag{3}$$

$$\gamma = p \tan\phi \tag{4}$$

where χ and γ are the effective magnetic susceptibility and the steerability, respectively. Herein, $\mathbf{L}_m$ is the magnetic torque, $\mathbf{M}$ the magnetic moment, $\mathbf{H}$ the external magnetic field, and V the volume of the magnetic material in the microswimmer. χ_0 is the isotropic component of the magnetic susceptibility, δ_{ik} the delta-symbol, $\mathbf{n}$ the vector of magnetic anisotropy, $\Delta\chi = \chi_{\parallel} - \chi_{\perp}$ the scalar parameter of magnetic anisotropy (in the case of easy-axis anisotropy, $\Delta\chi > 0$), $p = \kappa_{\perp}/\kappa_{\parallel} \geq 1$ the rotational viscous resistance ratio (depending on the aspect ratio of the prolate spheroid enclosing the helix) and ϕ the angel of magnetic anisotropy. Following ref.[46] , the maximal frequency below which the microswimmer propels synchronously with the magnetic field (i.e., step-out frequency) is formulated as:

$$f_{s\text{-}o} = \frac{\Delta\chi H^2 V}{\kappa_{\perp}} \frac{1+\gamma^2}{8\pi\gamma} \sin 2\phi \tag{5}$$

and the propulsion velocity in the synchronous regime is expressible by:

$$U = \left(2\pi R f_{s\text{-}o}\right) \cdot Ch \cdot \left(\frac{f}{f_{s\text{-}o}}\right) \left[1 - \left(\frac{2}{1+\gamma^2}\right)\left(\frac{f}{f_{s\text{-}o}}\right)^{-2}\left(1 + \sqrt{1 - \left(\frac{f}{f_{s\text{-}o}}\right)^2}\right)\right] \tag{6}$$

where R is the helix radius, and the steerability γ and chirality Ch (depending on the helix geometry only, see ref.[47]) serve as fitting parameters to approximate experimental data. Previously, superparamagnetic microswimmers have been reported in the form of artificial bacterial flagella (ABFs) fabricated through two-photon polymerization (TPP) using a magnetic polymer composite (MPC).[48,49] It was shown that helicity had a dominant role in determining how the microswimmers would magnetize, and furthermore, whether they could achieve corkscrew motion. According to Peyer et al.,[49] non-slender MPC microswimmers with a pitch angel (θ labeled in Figure S11, Supporting Information, the angle formed by the tangent of the helix and the helix axis; complementary angle of the helicity angle in ref.[49] larger than 60° are capable to perform effective propulsion without adjusted magnetic anisotropy in the process of TPP.[50] TS2-A-R1's capability of propulsive motion (Figure 4) is in accord with this finding, considering its typical pitch angle of ca. 67°. However, due to its unique porous hollow architecture, the actuator's exact steerability might differ much from that of an MPC microswimmer of equivalent helix geometry. To validate this assumption, we approximate the experimental data in the synchronous regime for TS2-A-R1 of different pitch numbers (n = 2, 4, 6) with theoretical predictions by Equation (6) (**Figure 5**). As a result, the respective steerability for the 2-pitch, 4-pitch, and 6-pitch TS2-A-R1 is found to be 13.5, 33.7, and 11.8, corresponding to a chirality value of 0.095, 0.056, and 0.053. These values suggest that TS2-A-R1 has achieved a higher propulsive capability in the context of superparamagnetic microswimmers, in comparison with the reference value of $\gamma = 9.3$ (corresponding to $Ch = 0.075$) owned by the recently developed MPC ABF (ref.[49]). In particular, for the 4-pitch TS2-A-R1 (the

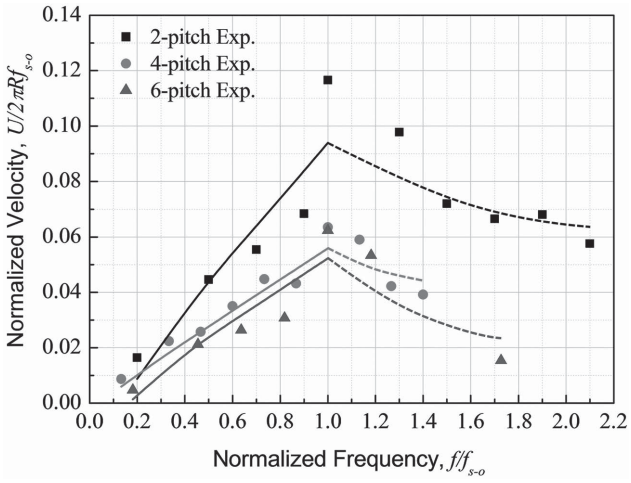

Figure 5. Dimensionless propulsion velocity of 2-pitch, 4-pitch, and 6-pitch TS2-A-R1 against rotating frequency normalized by the step-out frequency. The symbols (square, circle, and triangle) are experimental data points; solid lines the theoretical predictions by Equation (6); dashed lines the speculative velocity trends in the asynchronous regime (see ref.[47]. In our case, analytical solutions in this regime are not available).

reference MPC ABF is of 3-pitch), the steerability can be 3.6 times as large. A speculation is that the porous hollow architecture of TS2-A-R1 contributes to an overall more slender (ratio of the body length and filament thickness) body via building a virtually thinner filament (given that the magnetite shell is hydrophilic and water can enter the helical cavity), which according to the local drag theory will result in larger drag anisotropy (i.e., the difference of drag coefficients in the normal direction and tangent direction to an infinitesimal section of the filament). While for flagellar propulsion, the swimming speed is proportional to the magnitude of drag anisotropy.[51] For more evaluation of TS2-A-R1's swimming in terms of effective pitch, refer to the Supporting Information. In addition, it is worth mentioning that because TS2-A-R1's geometric parameters (e.g., body length, helix diameter, helicity) can be flexibly adjusted as needed through controlled cultivation of the *S. platensis*,[33,35,36] its propulsive capability could be further improved. Yet this is not the complete benefit of the geometry flexibility. For potential applications in vivo, such flexibility could help optimize our microswimmers for navigation in vessels or interstitial spaces of different dimensions. In the present work, the 2-pitch TS2-A-R1 as in Figure 4 has a comparable size (ca. three times as large) to the ABFs (a swarm of 80 000 in 400 µL 5% dextrose) recently reported to have successfully navigated the intraperitoneal cavity of a mouse through injection.[27]

3.2. Cytotoxicity Evaluation

The cytotoxicity of the microswimmers was also examined, which essentially determine whether targeted delivery in vivo with such microagents is safe and feasible. Specifically, MTT assay, a simple nonradioactive colorimetric method, was employed to test the cytotoxicity of TS2-A-R1. Samples were treated by sonication (20 kHz, 5 w cm^{-2}) for 20 min to obtain spindle-shaped magnetite NPs for MTT assay (see Section 3.4). Two groups of experiments were then independently carried out using the cervical cancer cell line SiHa and the mouse fibroblast cell line 3T3, and the results presented as cell viability against sample concentration and incubation time. As indicated in Figure S14 (Supporting Information), TS2-A-R1 shows negligible cytotoxicity for SiHa and 3T3 even for a high concentration of 0.4 µg mL^{-1} after 24 h incubation. For prolonged incubation of 48 h, significant reduction of cell viability is identified at 0.2 µg mL^{-1} for SiHa and at 0.4 µg mL^{-1} for 3T3. Nevertheless, the cell viability is still much higher than those tested for pure magnetite NPs of identical concentrations in the literature.[52] The enhanced cytocompatibility is believed to be correlated to the residual organic matter in TS2-A-R1, which can serve as a nutrition source for cells.[53]

3.3. Cargo Loading/Release

The capacity of the microswimmers for cargo loading was evaluated. The functionalization strategy has been employed as a versatile means to realize targeted delivery of molecular agents for helical microswimmers.[15,25–27] One of its primary advantages lies in the successful separation of the loading and transport processes. For this strategy, a large surface area of the vehicle is particularly favorable. In this respect, a significant progress was recently made by Peters et al., who developed robust twist-type helical microswimmers that achieved an over 150% increase in surface area without compromising the propulsion velocity.[54] However, we noted that the SSA,[1,55] a more general index to appraise structures' surface property, of their microswimmers is less satisfactory (Table S2, Supporting Information). In contrast, TS2-A-R1 overcomes this deficiency and is of an ultrahigh SSA with the value reaching 52.22 m^2 g^{-1}. The SSA value is calculated from the N_2 adsorption–desorption isotherms in Figure S9c (Supporting Information) using the typical Langmuir method. A double increase of SSA for our microswimmer is attributed to the hollow core architecture. And, the microscopic roughness and porous features of the shell contribute to further drastic amplification. With a variety of strategies available for the functionalization of magnetite devices as reported in the literature,[1,45,52] our proposed microswimmers are envisioned for broad biomedical applications as promising tools with high loading capacity for the delivery of various molecular therapeutic agents in vivo.

We pay particular attention to the hollow core/porous shell architecture of TS2-A-R1. Besides contributing to the increase of guest-loading capacity, it also enables the diffusion-based strategy of cargo loading/release.[55–58] This architecture of TS2-A-R1 provides large quantities of pathways (i.e., mesopores on the shell) connecting the external and the interior (hollow core) environments of the microswimmer. And the pore sizes (2–50 nm) make it ideal for encapsulation and loading of biomolecules or therapeutic NPs. Furthermore, by switching on and off these pathways, the microswimmer can be readily developed into an on-demand cargo loading/release system, which is highly favorable for targeted delivery. This function could be realized through coating stimuli-responsive matter such as polyelectrolytes and hydrogel on the surface of the microswimmer.[56,59] In this work, we tentatively explored

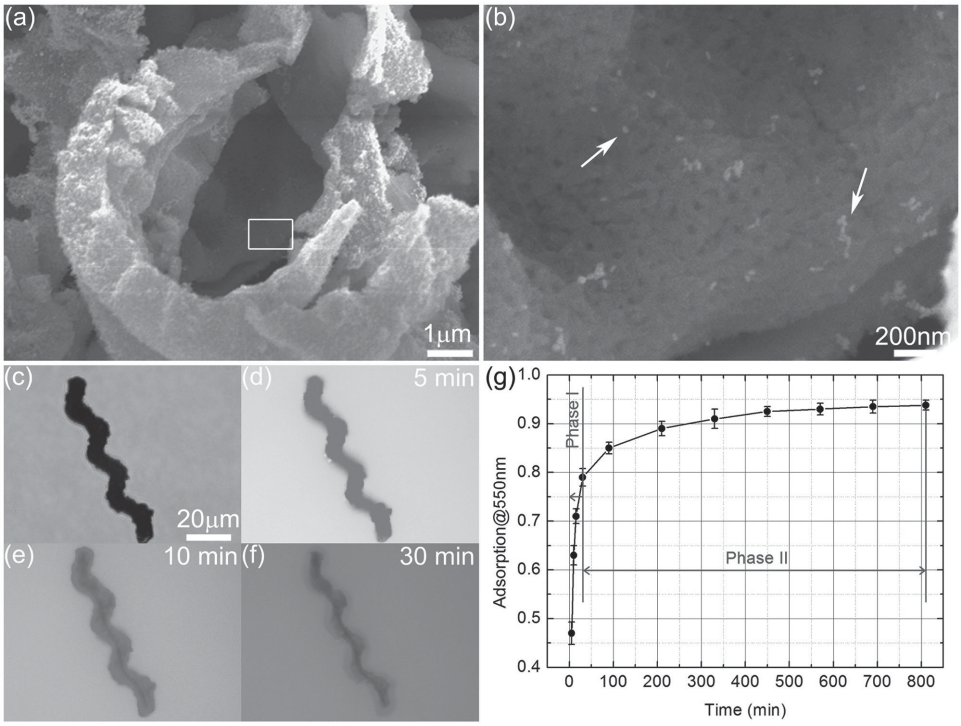

Figure 6. Cargo loading/release of TS2-A-R1. a) FESEM image of a cross-sectional fracture of TS2-A-R1 loaded with Au tracing nanorods. b) Magnified view of the white rectangular area marked in (a). The white arrows point to Au nanorods. c) Optical microscopy (bright-field) image of RhB-loaded TS2-A-R1. d–f) Fluorescence microscopy image sequence of the release of RhB tracing molecules from TS2-A-R1(excitation wavelength: 510–560 nm; exposure time: 200 ms; analog gain: 2.0×). g) Release profile of RhB from TS2-A-R1. (c–f) share the same scale bar as in (c), which is 20 μm.

the diffusion-based processes of cargo loading and release using Au tracing nanorods of ca. 21 nm in diameter and 36 nm in length (Figure S15a, Supporting Information) and RhB tracing molecules, respectively. The results of cargo loading are shown in **Figure 6**a,b by a cross-sectional fracture of Au-loaded TS2-A-R1, where rod-like NPs that have never been found before Au-loading can now be clearly observed inside the microswimmer. EDX analysis confirmed the existence of Au in TS2-A-R1 after the loading process (Figure 15b, Supporting Information). With the aforementioned information, we strongly believe that those NPs are Au nanorods from the loading process via diffusion. The process of cargo release is shown in Figure 6c–f using RhB-loaded TS2-A-R1. The RhB molecule is chosen as the tracer because of its stable fluorescence features. In the experiment, we employed green light with a wavelength of 510–560 nm to excite the red fluorescence emission of RhB. By detecting the red fluorescence signal, the diffusion process was illustrated as in Figure 6d–f. The time-lapse sequence indicates that the RhB molecules gradually diffused into the external solution from the interior of TS2-A-R1, consequently decreasing the intensity of red fluorescence signal in TS2-A-R1. This process was also quantitatively presented by the release profile of RhB (Figure 6g) through monitoring the absorption intensity at 550 nm at defined time intervals. The release profile can be divided into two phases with distinct rates of change. Phase I exhibits high rate of change due to rapid release of RhB, while the rate is much smaller in Phase II, indicating slow release. Given the microstructural properties of TS2-A-R1, the release in Phase I and Phase II is mainly attributed to RhB diffused from the hollow core and the mesoporous NPs, respectively.

3.4. Structural Disassembly

Interestingly, during experiments of producing TS2-A-R1 segmentations via sonication, it was observed that multilevel structural disassembly can be realized by controlling the time of ultrasound treatment. This means that the outer shell aggregated by mesoporous magnetite NPs is susceptible to ultrasonic disruption and can be decomposed by localized shock waves induced by sonication,[60] thus suggesting structural versatility of our proposed microswimmers (see the schematic in **Figure 7**a). Figure 7c–e shows FESEM images of TS2-A-R1 samples subjected to low-intensity sonication (20 kHz, 0.7 w cm^{-2}) for 1 min, 5 min, and 20 min, respectively. The results show that TS2-A-R1 is gradually disassembled to different levels as the treatment time increases (Figure 7b–d) and eventually shattered into individual spindle-shaped magnetite NPs for a sonication time of 20 min (Figure 7e). With sonication of higher intensity, the decomposition process can be speeded up and the time required for the microhelices to evolve into segmentations/NPs significantly reduced. The feasibility of structural disassembly of our microswimmers provides a solution for potential blockage of helical microswimmers inside capillaries in vivo. In this sense, with the support of surgical high-intensity focused ultrasound (HIFU, >5 w cm^{-2}) technique,[61] safer targeted delivery is expected. On the other hand,

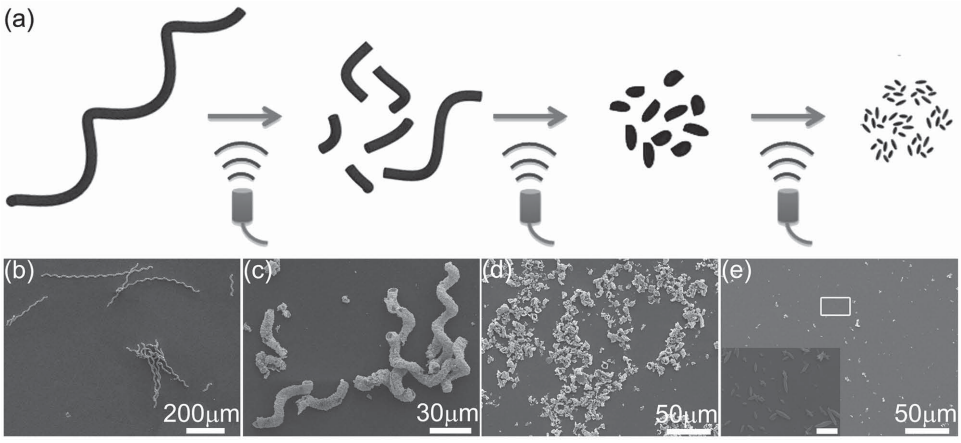

Figure 7. Structural disassembly of TS2-A-R1 with ultrasound treatment. a) Schematic of the multilevel disassembly process. b–e) FESEM images of TS2-A-R1 subject to sonication of 0, 1, 5, and 20 min, respectively. Inset in (e): Enlarged view of the white rectangular area marked in (e). The scale bar in the inset is 500 nm.

high-dose release of drug required by some therapies can be facilitated by instantaneous comminution of drug-loaded TS2-A-R1 via HIFU. Furthermore, simultaneous release of several therapeutic agents is possible. For instance, the hollow core can be used to contain one drug agent via diffusion-based cargo loading, while the mesoporous magnetite NPs on the shell can serve as nanocarriers for loading another drug via functionalization. When exposed to HIFU after arriving the targeted organs or issues, the microswimmers are shattered and both agents can be released at once.

4. Conclusion

In this work, we report a method of biotemplated synthesis for the cost-effective mass-production of magnetite porous hollow helical microswimmers. Three key steps, i.e., precursor deposition, annealing treatment, and reduction processing, are involved in the synthesis. The as-obtained helical microswimmers are superparamagnetic and capable of performing controlled locomotion under a low-strength rotating magnetic field. Furthermore, they show excellent cytocompatibility via MTT assay using SiHa and 3T3 cell lines. Microscopy and other testing techniques reveal the intrinsic micro-/nanostructures that lead to the superior characteristics of our microswimmer for targeted delivery, including a super-high SSA, an architecture of diffusion-based loading/release capability, and the feasibility of structural disassembly using ultrasound. All these desirable properties suggest a versatile microrobotic tool with high loading capacity for biomedical applications in vivo.

5. Experimental Section

Materials: The *S. platensis* was cultivated in standard Zarrouk medium[29] at College of Resources and Environment, Qingdao Agricultural University, China. To exclude the influence of the cultivation medium, the *S. platensis* was washed clean (three times) before being used for experiments. Ferric chloride ($FeCl_3$) and ferrous chloride tetrahydrate ($FeCl_2{\cdot}4H_2O$) were purchased from Acros Organics (Thermo Fisher Scientific Inc., USA) and Aladdin (China), respectively; Absolute ethanol from EMSURE (Germany); MTT, RhB, and dimethyl sulfoxide (DMSO) from Sigma–Aldrich (USA); and all reagents for cell culture from Gibco (USA). The cervical cancer cell line SiHa and the mouse fibroblast cell line 3T3 were obtained from ATCC (USA). Ultrahigh purity N_2 was provided by Linde HKO Limited (Hong Kong). All regents were used without further purification.

Fabrication of Spirulina-Templated Microswimmers: The first step is to deposit magnetite precursor on the surface of the *S. platensis*. Through tentative experiments, the optimum conditions were determined as: synthesis in a mixed solution of $FeCl_2$ and $FeCl_3$ (molar ratio in 2:1) at 65 °C with the protection of ultrahigh-purity N_2. 5 mg dried *S. platensis* was added to 50 mL mixed solution of $FeCl_2{\cdot}4H_2O$ (1.0296 g) and $FeCl_3$ (0.4225 g). Gentle stirring was then employed to avoid the formation of large aggregates and ensure homogeneous deposition of the precursor on the surfaces. After a respective treatment time of 0.5, 1, 2, and 3 h, four groups of samples were extracted from the mixed solution by centrifugation. Subsequently, we proceeded with absolute ethanol-assisted drying treatment in a vacuum drying oven. The dried products were then annealed at 550 °C for 1 h with no gas protection. All annealed samples were cooled in the furnace to reduce potential damage caused by residual stress. As the last step, the annealed products were reduced under a hydrogen/argon (volume ration, 1:9) flow at 550 °C.

Characterization of Microstructural, Thermal, and Magnetic Properties: Optical image was taken by an OLYMPUS optical microscope connected to PC with a CCD camera. FESEM images were acquired using FEI Quanta 400F microscope with an accelerating voltage of 10 kV. To enhance the conductivity, all samples unless specified went through gold sputtering at 10 mA for 45 s using a SC 502 Ion Sputter Coating Machine (POLARON). Element analysis was carried out with an EDX analyzer (operated with 20 kV) mounted on the FEI Quanta 400F. XRD test was conducted on a Smartlab (Rigaku) diffractometer using Cu target (40 kV, 40 mA). TEM images were acquired using a FEI Tecnai Spirit electron microscopy with an accelerating voltage of 200 kV. N_2 adsorption–desorption isotherms were measured on a Nova 1200e instrument at liquid-nitrogen temperature using ultrapure nitrogen gas as the adsorbate (Quantachrome Instruments). Measurements were made after degassing treatment for 6 h at 473 K with N_2 flow. The SSA was calculated based on the typical Langmuir method. And, the distribution of pore size was calculated based on the Barrett-Joyner-Halenda (BJH) method. The disassembly experiments were conducted using Ultrasonic Processors (VCX 750, SONICS) equipped with 13 mm Titanium alloy (Ti-6Al-4V) probe. For three groups of samples, the ultrasound treatment (20 kHz, 0.7 w cm^{-2}) was conducted in DI water for 1, 5, and 20 min, respectively. Typical TG analysis was

conducted using (TGA6, PerkinElmer) with a heating rate of 10 °C min^{-1}. Magnetic properties were tested using a VSM (PPMS Model 6000 Quantum Design).

Characterization of Swimming Performance: The swimming test was carried out in homogeneous rotating magnetic fields generated by a tri-axial Helmholtz coil system. The microswimmers were put inside a tank filled with DI water, which was placed in the central workspace of the coil setup. An optical microscope connected to PC with a CCD camera was mounted above the tank for visual tracking and data recording. More details of the experimental setup can be found in ref.[7].

Cargo Loading/Release: The cargo loading and release experiments of microswimmers TS2-A-R1 (weight of dried samples, 1 mg) were carried out in CTAB stabilized Au-nanorod colloids and concentrated RhB aqueous solution (40 mg in 200 mL DI water), respectively. The loading process lasted for 24 h with mild shaking (180 rpm) produced by an orbital shaker (N-BioTek). The obtained products were rinsed clean (>5 times) using DI water with the aid of a permanent magnet. Au-loaded TS2-A-R1 samples were sonicated (20 kHz, 0.7 w cm^{-2}) for 1 min into segmentations to produce the cross-sectional fractures for FESEM imaging. The release of RhB from TS2-A-R1 was monitored through respective imaging at 5, 10, and 30 min using Nikon Inverted Fluorescence Microscope TS-100 (with bright-field functions) at 510–560 nm excitation wavelength. And the absorption intensity of the RhB release profile was collected using Multiskan GO Microplate Spectrophotometer (Thermo Scientific, USA).

Cell Culture and Subculture: The cervical cancer cell line SiHa was cultured with minimum essential media (MEM) at 37 °C in a 5% CO_2-95% air humidified atmosphere. When the cell confluence reached ca. 75%–80%, the cells were washed by sterile phosphate-buffered saline (PBS). Next, the trypsin was neutralized (Invitrogen, CA USA) by full medium and washed it by PBS. Then the cells were collected via centrifugation (1000 g for 5 min). Subsequently, the cell pellet was resuspended with fresh full medium and passaged to four plastic tissue culture dishes (100 mm). Lastly, they were incubated at 37 °C in a 5% CO_2-95% air humidified atmosphere for proliferation. The mouse fibroblast cell line 3T3 was cultured with the same protocol.

MTT Assay: MTT assay was performed for TS2-A-R1 with cervical cancer cell line SiHa and the mouse fibroblast cell line 3T3. All experiments were repeated three times for verification. SiHa and 3T3 cells were separately seeded into 96-well (4000 cells per well) culture plates (Invitrogen) and cultured at 37 °C in a 5% CO_2-95% air humidified atmosphere. After 24 h incubation for cells to adhere, the culture medium was replaced with new medium containing TS2-A-R1 of concentrations 0, 25, 50, 100, 200, and 400 μg mL^{-1}, respectively (six replicate wells for each concentration, with a final volume of 100 μL per well). After another 24 or 48 h incubation, the culture medium was carefully removed and the cells were washed twice with PBS. Subsequently, 150 μL (0.5 mg mL^{-1}) MTT were added. After incubation for 4 h, the culture medium was again carefully removed, and 150 μL DMSO per well was added, followed 10 min shaking on a horizontal shaker. Absorbance was read using enzyme-labeling analysis equipment (Biotek Synergy 2, BioTek, USA) at 570 nm. The average absorbance yields results of cell viability.

Supporting Information

Supporting Information is available from the Wiley Online Library or from the author.

Acknowledgements

The authors gratefully thank Prof. Jianfang Wang and Miss. Nina Jiang (Department of Physics, the Chinese University of Hong Kong) for providing Au nanorods, Prof. Douglas Yung, Mr. Nelson So (Division of Biomedical Engineering, the Chinese University of Hong Kong) and Prof. Quan Li (Department of Physics, the Chinese University of Hong Kong) for providing instruments to prepare materials and Mr. Xin Wang (College of Marine Science and Engineering, Qingdao Agricultural University) for the cultivation of the *S. platensis*. Also, our thanks are extended to Ms. Jiao Chen (Department of Obstetrics and Gynaecology, the Chinese University of Hong Kong), Mr. Qian Li, Mr. Andrew Li, and Mr. Man Hau Yeung (Department of Physics, The Chinese University of Hong Kong, Hong Kong) for their discussions and help with the characterization of material properties. This research is financially supported by the early career scheme (ECS) grant, General Research Fund (GRF) and PROCORE - France/Hong Kong Joint Research Scheme from the Research Grants Council (RGC) of Hong Kong with Project No. 439113, 14209514 and F-CUHK408/13, respectively, as well as the National Natural Science Funds of China for Young Scholar with the Project No. 61305124.

Received: June 2, 2015
Revised: July 1, 2015
Published online: July 24, 2015

[1] A. K. Gupta, M. Gupta, *Biomaterials* **2005**, *26*, 3995.
[2] K. Cho, X. Wang, S. Nie, Z. G. Chen, D. M. Shin, *Clin. Cancer Res.* **2008**, *14*, 1310.
[3] B. J. Nelson, I. K. Kaliakatsos, J. J. Abbott, *Annu. Rev. Biomed. Eng.* **2010**, *12*, 55.
[4] H. Koo, M. S. Huh, I. C. Sun, S. H. Yuk, K. Choi, K. Kim, I. C. Kwon, *Acc. Chem. Res.* **2011**, *44*, 1018.
[5] J. Wang, W. Gao, *ACS Nano* **2012**, *6*, 5745.
[6] W. F. Paxton, K. C. Kistler, C. C. Olmeda, A. Sen, S. K. St Angelo, Y. Cao, T. E. Mallouk, P. E. Lammert, V. H. Crespi, *J. Am. Chem. Soc.* **2004**, *126*, 13424.
[7] L. Zhang, J. J. Abbott, L. Dong, B. E. Kratochvil, D. Bell, B. J. Nelson, *Appl. Phys. Lett.* **2009**, *94*, 064107.
[8] D. Kagan, M. J. Benchimol, J. C. Claussen, E. Chuluun-Erdene, S. Esener, J. Wang, *Angew. Chem. Int. Ed.* **2012**, *51*, 7519.
[9] W. Gao, D. Kagan, O. S. Pak, C. Clawson, S. Campuzano, E. Chuluun-Erdene, E. Shipton, E. E. Fullerton, L. Zhang, E. Lauga, J. Wang, *Small* **2012**, *8*, 460.
[10] S. Taherkhani, M. Mohammadi, J. Daoud, S. Martel, M. Tabrizian, *ACS Nano* **2014**, *8*, 5049.
[11] J. J. Abbott, K. E. Peyer, M. C. Lagomarsino, L. Zhang, L. Dong, I. K. Kaliakatsos, B. J. Nelson, *Int. J. Robot. Res.* **2009**, *28*, 1434.
[12] R. S. Rikken, R. J. Nolte, J. C. Maan, J. C. Van Hest, D. A. Wilson, P. C. Christianen, *Soft Matter* **2014**, *10*, 1295.
[13] E. M. Purcell, *Am. J. Phys.* **1977**, *45*, 3.
[14] H. C. Berg, D. A. Brown, *Nature* **1972**, *239*, 500.
[15] A. Ghosh, P. Fischer, *Nano Lett.* **2009**, *9*, 2243.
[16] S. Schuerle, S. Pane, E. Pellicer, J. Sort, M. D. Baro, B. J. Nelson, *Small* **2012**, *8*, 1498.
[17] S. Tottori, L. Zhang, F. Qiu, K. K. Krawczyk, A. Franco-Obregon, B. J. Nelson, *Adv. Mater.* **2012**, *24*, 811.
[18] W. Gao, X. Feng, A. Pei, C. R. Kane, R. Tam, C. Hennessy, J. Wang, *Nano Lett.* **2014**, *14*, 305.
[19] P. L. Venugopalan, R. Sai, Y. Chandorkar, B. Basu, S. Shivashankar, A. Ghosh, *Nano Lett.* **2014**, *14*, 1968.
[20] D. Schamel, A. G. Mark, J. G. Gibbs, C. Miksch, K. I. Morozov, A. M. Leshansky, P. Fischer, *ACS Nano* **2014**, *8*, 8794.
[21] K. Ishiyama, M. Sendoh, K. I. Arai, *J. Magn. Magn. Mater.* **2002**, *242*, 41.
[22] B. J. Nelson, K. E. Peyer, *ACS Nano* **2014**, *8*, 8718.
[23] K. E. Peyer, L. Zhang, B. J. Nelson, *Appl. Phys. Lett.* **2011**, *99*, 174101.
[24] T.-Y. Huang, F. Qiu, H.-W. Tung, X.-B. Chen, B. J. Nelson, M. S. Sakar, *Appl. Phys. Lett.* **2014**, *105*, 114102.

[25] R. Mhanna, F. Qiu, L. Zhang, Y. Ding, K. Sugihara, M. Zenobi-Wong, B. J. Nelson, *Small* **2014**, *10*, 1953.
[26] F. Qiu, S. Fujita, R. Mhanna, L. Zhang, B. R. Simona, B. J. Nelson, *Adv. Funct. Mater.* **2015**, *25*, 1666.
[27] A. Servant, F. Qiu, M. Mazza, K. Kostarelos, B. J. Nelson, *Adv. Mater.* **2015**, *27*, 2981.
[28] J. D. Watson, F. H. C. Crick, *Nature* **1953**, *171*, 737.
[29] C. Zarrouk, *Ph.D. Thesis*, University of Paris (Paris, France) **1966**.
[30] R. Mogul, J. J. G. Kelly, M. L. Cable, A. F. Hebard, *Mater. Lett.* **2006**, *60*, 19.
[31] K. Muto, H. Y. Kubota, *Cell Motil. Cytoskeleton* **2009**, *66*, 281.
[32] A. Belay, Y. Ota, K. Miyakawa, H. Shimamatsu, *J. Appl. Phycol.* **1993**, *5*, 235.
[33] C. Van Eykelenburg, A. Fuchs, *Naturwissenschaften* **1980**, *67*, 200.
[34] O. Ciferri, *Microbiol. Rev.* **1983**, *47*, 551.
[35] M. Muhling, N. Harris, A. Belay, B. A. Whitton, *J. Phycol.* **2003**, *39*, 360.
[36] Z. Ma, K. Gao, *Planta* **2009**, *230*, 329.
[37] B. Chen, T. Z. Zhan, Z. Y. Lian, D. Y. Zhang, *Sci. China Ser. E* **2008**, *51*, 591.
[38] D. Y. Zhang, W. Q. Zhang, J. Cai, *Sci. China Technol. Sci.* **2011**, *54*, 1275.
[39] Y. Oaki, N. Yagita, H. Imai, *Chem. Eur. J.* **2012**, *18*, 110.
[40] S. Behrens, J. Wu, W. Habicht, E. Unger, *Chem. Mater.* **2004**, *16*, 3085.
[41] A. K. Boal, T. J. Headley, R. G. Tissot, B. C. Bunker, *Adv. Funct. Mater.* **2004**, *14*, 19.
[42] F. C. Meldrum, H. Clfen, *Chem. Rev.* **2008**, *108*, 4332, 1255.
[43] T. J. Zhang, W. Wang, D. Y. Zhang, X. X. Zhang, Y. R. Ma, Y. L. Zhou, L. M. Qi, *Adv. Funct. Mater.* **2010**, *20*, 1152.
[44] S. A. Davis, S. L. Burkett, N. H. Mendelson, S. Mann, *Nature* **1997**, *385*, 420.
[45] A. H. Lu, E. L. Salabas, F. Schuth, *Angew. Chem. Int. Ed.* **2007**, *46*, 1222.
[46] K. I. Morozov, A. M. Leshansky, *Nanoscale* **2014**, *6*, 12142.
[47] K. I. Morozov, A. M. Leshansky, *Nanoscale* **2014**, *6*, 1580.
[48] M. Suter, O. Ergeneman, J. Zurcher, C. Moitzi, S. Pane, T. Rudin, S. E. Pratsinis, B. J. Nelson, C. Hierold, *Sens. Actuators, B* **2011**, *156*, 433.
[49] K. E. Peyer, E. C. Siringil, L. Zhang, M. Suter, B. J. Nelson, in *Living Machines*, (Eds: N. F. Lepora, A. Mura, H. G. Krapp, P. F. M. J. Veschure, T. J. Prescott), Springer-Verlag, Berlin, Germany, **2013**, pp. 216–227.
[50] C. Peters, O. Ergeneman, B. J. Nelson, C. Hierold, presented at *IEEE 26th Int. Conf. on Micro Electro Mechanical Systems*, Taipei, Taiwan, January **2013**, 564.
[51] E. Lauga, T. R. Powers, *Rep. Prog. Phys.* **2009**, *72*, 096601.
[52] A. K. Gupta, A. S. Curtis, *Biomaterials* **2004**, *25*, 3029.
[53] Y. D. Tu, Z. Zhou, R. J. Yan, Y. P. Gan, W. Z. Huang, X. X. Weng, H. Huang, W. K. Zhang, X. Y. Tao, *RSC Adv.* **2012**, *2*, 10585.
[54] C. Peters, O. Ergeneman, P. D. W. Garcia, M. Muller, S. Pane, B. J. Nelson, C. Hierold, *Adv. Funct. Mater.* **2014**, *24*, 5269.
[55] Y. Chen, H. Chen, D. Zeng, Y. Tian, F. Chen, J. Feng, J. Shi, *ACS Nano* **2010**, *4*, 6001.
[56] Y. Zhu, J. Shi, W. Shen, X. Dong, J. Feng, M. Ruan, Y. Li, *Angew. Chem. Int. Ed.* **2005**, *44*, 5083.
[57] L. Li, J. Ding, J. M. Xue, *Chem. Mater.* **2009**, *21*, 3629.
[58] Y. Chen, C. Chu, Y. Zhou, Y. Ru, H. Chen, F. Chen, Q. He, Y. Zhang, L. Zhang, J. Shi, *Small* **2011**, *7*, 2935.
[59] J. Kopecek, *Biomaterials* **2007**, *28*, 5185.
[60] J. S. Taurozzi, V. A. Hackley, M. R. Wiesner, *Nanotoxicology* **2011**, *5*, 711.
[61] G. Ter Haar, *Eur. J. Ultrasound* **1999**, *9*, 3.